Geophys. J. Int. (1992) **108**, 16–34

Seismic traveltime inversion for 2-D crustal velocity structure

C. A. Zelt* and R. B. Smith
Department of Geology and Geophysics, University of Utah, Salt Lake City, UT USA 84112

Accepted 1991 May 23. Received 1991 May 20; in original form 1990 November 6

SUMMARY

A method of seismic traveltime inversion for simultaneous determination of 2-D velocity and interface structure is presented that is applicable to any type of body-wave seismic data. The advantage of inversion, as opposed to trial-and-error forward modelling, is that it provides estimates of model parameter resolution, uncertainty and non-uniqueness, and an assurance that the data have been fit according to a specified norm. In addition, the time required to interpret data is significantly reduced. The inversion scheme is iterative and is based on a model parametrization and a method of ray tracing suited to the forward step of an inverse approach. The number and position of velocity and boundary nodes can be adapted to the shot–receiver geometry and subsurface ray coverage, and to the complexity of the near-surface. The model parametrization also allows ancillary amplitude information to be used to constrain model features not adequately resolved by the traveltime data alone. The method of ray tracing uses an efficient numerical solution of the ray tracing equations, an automatic determination of take-off angles, and a simulation of smooth layer boundaries that yields more stable inversion results. The partial derivatives of traveltime with respect to velocity and the depth of boundary nodes are calculated analytically during ray tracing and a damped least-squares technique is used to determine the updated parameter values, both velocities and boundary depths simultaneously. The stopping criteria and optimum number of velocity and boundary nodes are based on the trade-off between RMS traveltime residual and parameter resolution, as well as the ability to trace rays to all observations. Methods for estimating spatial resolution and absolute parameter uncertainty are presented. An example using synthetic data demonstrates the algorithm's accuracy, rapid convergence and sensitivity to realistic noise levels. An inversion of refraction and wide-angle reflection traveltimes from the 1986 IRIS–PASSCAL Nevada, USA (Basin and Range province) seismic experiment illustrates the methodology and practical considerations necessary for handling real data. A comparison of our final 2-D velocity model with results from studies using other 1-D and 2-D forward and inverse methods serves as a check on the validity of the inversion scheme and provides estimates of parameter uncertainties that account for the bias introduced by the modelling approach and the interpreter.

Key words: inversion, model parametrization, ray tracing, seismic, traveltime, velocity.

1 INTRODUCTION

The interpretation of crustal refraction/wide-angle reflection data for 2-D velocity structure often involves laborious trial-and-error ray-trace forward modelling (e.g. Catchings & Mooney 1988; Boland & Ellis 1989; Henry *et al.* 1990). Ray tracing algorithms for forward modelling such as those developed by Červený, Molotkov & Pšenčík (1977), McMechan & Mooney (1980) or Spence, Whittall & Clowes (1984) are often used. The theoretical response of a laterally heterogeneous medium is repeatedly compared with observed data until a velocity model is constructed that provides a suitable match between the calculated and observed response. An experienced interpreter can often

* Now at: Geological Survey of Canada, 1 Observatory Crescent, Ottawa, Canada K1A OY3.

assess how relevant model parameters need to be adjusted to improve the fit along one or two traveltime branches for one or a few shots simultaneously. Nevertheless, forward modelling remains a time-consuming process, regardless of computer speed, due to the many iterations normally required and the necessary human interaction. For seismic experiments that consist of numerous shots along a single line, it may be impossible through trial-and-error modelling to construct a model that fits the data within acceptable limits. In addition, forward modelling cannot provide quantitative estimates of model parameter uncertainty and resolution or a sense of model non-uniqueness. Finally, forward modelling cannot assure that the data have been fit to minimize a particular norm.

In contrast to the limitations of forward modelling, generalized linear inversion can provide estimates of parameter uncertainty, resolution and non-uniqueness as well as an assurance that a local minimum of a particular norm is achieved. Methods for the inversion of crustal refraction/wide-angle reflection traveltimes in 2-D media have been developed by Spence (1984), Huang, Spencer & Green (1986), Firbas (1987) and Lutter, Nowack & Braile (1990). These methods employ ray tracing algorithms that were originally designed for forward modelling only. This limits the effectiveness of these approaches since the forward algorithm should be suited to the special needs of the inverse problem: a flexible model parametrization that uses a minimum number of independent parameters and a computationally efficient and robust method of ray tracing.

This paper presents a technique for inverting traveltimes to obtain 2-D velocity and interface structure simultaneously, in which the model parametrization and method of ray tracing are suited to the forward step of an inversion algorithm. The method is applicable to any set of traveltimes for which forward modelling is possible, regardless of the shot–receiver geometry or data quality, since the forward step is equivalent to trial-and-error forward modelling.

The non-linearity of traveltime inversion makes a starting model and iterative approach necessary, thus, requiring a practical and efficient forward step. The model parametrization presented here uses layers composed of variable-sized blocks in which a minimum number of independent parameters are required to represent typical crustal and upper mantle models. The number and position of model parameters (velocity and boundary nodes) specifying each layer can be completely general and thereby adapted to the subsurface resolution of the data, and also allows the surface relief and near-surface velocity variations to be incorporated into the model. The method of ray tracing is by an efficient numerical solution of the 2-D ray tracing equations coupled with an automatic determination of ray take-off angles. The instability associated with a blocky model parametrization is reduced by applying a smooth layer boundary simulation. The first step of the inversion is the analytic calculation of partial derivatives of traveltime with respect to the model velocities and the vertical position of boundary nodes. These partial derivatives are calculated during ray tracing and may correspond to any arrival identified in the observed seismic traveltime data (e.g. refraction, reflection, head wave, multiple). Traveltimes and partial derivatives are interpolated across ray endpoints to the receiver locations, avoiding the need for two-point ray tracing. Damped least-squares inversion is used to determine the updated model parameters of those selected for adjustment, both velocities and boundary nodes simultaneously.

The algorithm is suited for multishot crustal seismic data that might normally be forward modelled because the shot and/or receiver density does not permit the application of high-resolution or wavefield inversion techniques. It is also useful for obtaining preliminary models for these methods or as an aid in determining optimal shot–receiver geometries during experiment planning. The efficiency of the inversion routine and the typical number of shots and receivers used in crustal seismic experiments allows it to operate effectively in a computer workstation environment. After a description of the model parametrization and method of ray tracing and inversion, the routine is illustrated and tested with synthetic data. This is followed by an application to the north–south line of the 1986 IRIS–PASSCAL, Nevada, seismic experiment and a comparison of these results with other 1-D and 2-D interpretations.

2 MODEL PARAMETRIZATION

A ray tracing algorithm and its effectiveness for use in inverse modelling are most strongly characterized by the model parametrization. The parametrization presented here is a modification of that used by Zelt & Ellis (1988): a layered, variable-block-size representation of 2-D isotropic velocity structure (Fig. 1). Each layer boundary is specified by an arbitrary number and spacing of boundary nodes connected by linear interpolation; the number and position of nodes may differ for each boundary. Layer boundaries must cross the model from left to right without crossing another boundary. A single node may be used to represent a horizontal boundary, whereas detailed topographic relief may be specified by multiple nodes. Within each layer, the *P*-wave velocity field is specified by an arbitrary number and spacing of upper and lower layer velocity points. The number and position of upper layer velocity points may be different from the lower layer velocity points and the

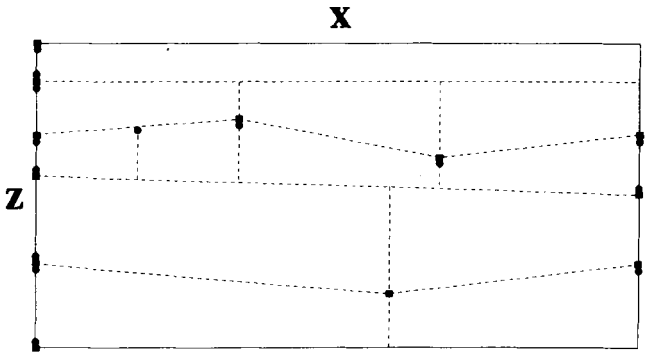

Figure 1. Example of the velocity model parametrization. The five-layer model is defined by 26 independent model parameters: 12 boundary nodes (squares) and 14 velocity points (circles). For the purpose of ray tracing, the model is automatically divided into 12 trapezoidal blocks. Note that (1) the first layer is laterally homogeneous, (2) the second layer has a constant velocity, and (3) the boundary between the third and fourth layers has no associated velocity discontinuity.

velocity points in other layers (Fig. 1). The complete velocity field within each layer is defined such that the velocity varies linearly with position along the upper and lower layer boundaries between the specified points and linearly between the upper and lower boundaries in the vertical direction. A constant velocity along an upper or lower layer boundary across the full length of the model is specified by a single velocity point, and a constant-velocity layer is specified by a single velocity value for the layer.

For the purpose of ray tracing, each layer is divided laterally into trapezoidal blocks separated by vertical boundaries that are included automatically wherever there is an upper or lower layer boundary node or velocity point (Fig. 1). Although velocity discontinuities may exist across layer boundaries, the velocity is continuous laterally within layers across the vertical boundaries. A layer boundary can represent an interface without an associated velocity discontinuity by applying the velocity at the base of the upper layer to the velocity at the top of the lower layer.

For a model trapezoid (Fig. 2) that has four boundaries in the x–z plane defined by

$$x = x_1, \quad x = x_2, \quad z = s_1 x + b_1, \quad z = s_2 x + b_2,$$

and four corner velocities v_1, v_2, v_3 and v_4, the P-wave velocity, v, within the trapezoid is

$$v(x, z) = \frac{(c_1 x + c_2 x^2 + c_3 z + c_4 xz + c_5)}{(c_6 x + c_7)}, \tag{1}$$

where the coefficients, c_i, are linear combinations of the corner velocities;

$$\begin{aligned}
c_1 &= s_2(x_2 v_1 - x_1 v_2) + b_2(v_2 - v_1) \\
&\quad - s_1(x_2 v_3 - x_1 v_4) - b_1(v_4 - v_3), \\
c_2 &= s_2(v_2 - v_1) - s_1(v_4 - v_3), \\
c_3 &= x_1 v_2 - x_2 v_1 + x_2 v_3 - x_1 v_4, \\
c_4 &= v_1 - v_2 + v_4 - v_3, \\
c_5 &= b_2(x_2 v_1 - x_1 v_2) - b_1(x_2 v_3 - x_1 v_4), \\
c_6 &= (s_2 - s_1)(x_2 - x_1), \\
c_7 &= (b_2 - b_1)(x_2 - x_1).
\end{aligned} \tag{2}$$

The corner velocities v_1, v_2, v_3 and v_4, in general, represent values linearly interpolated from the user-specified values. A simpler function of x and z than (1) cannot provide the desired velocity field that varies linearly with position along the four sides of a trapezoid. The coefficients $c_1, c_2, \ldots, c_7$ are pre-calculated for all trapezoids prior to ray tracing.

There are a number of advantages to a parametrization of the model that consists of a layered, irregular network of trapezoids based on linear interpolation: (1) the shape of each trapezoid and its velocity field can be sufficiently general so that a minimum number of trapezoids are required to represent complex crustal models; (2) a layered model has enough 'structure' to make the bookkeeping associated with ray tracing relatively simple and efficient, and specification of the model and ray groups is more straightforward; (3) linear interpolation between all boundary nodes and velocity points assures that the model is predictable and well behaved; (4) the layered network allows any single boundary node or velocity point to be adjusted and the model remains consistent and well defined; and (5) an irregular network can be adapted to suit the subsurface ray coverage and resolution of the observed data.

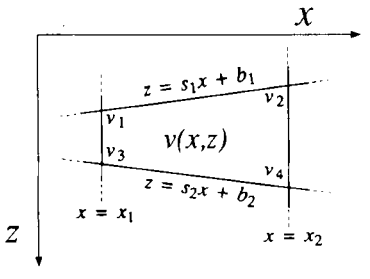

Figure 2. The velocity distribution, $v(x, z)$, inside a model trapezoid is given by (1).

The parametrization allows layers to be reduced to a zero thickness so that pinch-outs and isolated bodies can be included in the model. In this case, the trapezoid(s) adjacent to the pinch-out will be a three-sided block with its velocity field defined by three corner velocities instead of four.

3 RAY TRACING

Rays are traced through the velocity model using zero-order asymptotic ray theory by solving the ray tracing equations numerically (see Červený *et al.* 1977). The 2-D ray tracing equations are a pair of first-order ordinary differential equations that can be written in two forms:

$$\frac{dz}{dx} = \operatorname{cotan}\theta, \qquad \frac{d\theta}{dx} = \frac{(v_z - v_x \operatorname{cotan}\theta)}{v}, \tag{3a}$$

or

$$\frac{dx}{dz} = \tan\theta, \qquad \frac{d\theta}{dz} = \frac{(v_z \tan\theta - v_x)}{v}, \tag{3b}$$

with initial conditions

$$x = x_0, \quad z = z_0, \quad \theta = \theta_0$$

(Červený *et al.* 1977, equations 3.19 and 3.19′). The variable θ is the angle between the tangent to the ray and the z axis, v is the wave velocity and v_x and v_z are partial derivatives of velocity with respect to the x and z coordinates, respectively (z is positive downward). The point (x_0, z_0) is the source location and θ_0 is the ray take-off angle. System (3a) is solved with x as the integration variable when the ray path is near-horizontal, and system (3b) is solved with z as the integration variable when the ray path is near-vertical. A Runge–Kutta method (Sheriff & Geldart 1983) with error control is used to solve these systems as suggested by Červený *et al.* (1977). To complete the basic ray tracing algorithm, Snell's law is applied at the intersection of a ray with a layer boundary.

3.1 Ray step length

The ray step length, Δ, used to solve (3a) or (3b) is an increment in the x or z direction, respectively. The step length is adjusted at each point along the ray path according to the relationship

$$\Delta = \frac{\alpha v}{|v_x| + |v_z|} \tag{4}$$

where α is a user-specified constant. Equation (4) adjusts

the step length according to the local derivative of the velocity field to avoid unnecessarily small step lengths when the ray bending is small and the potential inaccuracy of using a large step length when the bending is large.

Within trapezoids that have a constant velocity gradient, the ray paths are circular arcs; equation (4) ensures that any ray path, if extrapolated to a full circle in such a trapezoid, would be defined by at least $2\pi/\alpha$ step lengths. Since the velocity, given by (1), and its partial derivatives are analytic functions of position, (3a) and (3b) can, in conjunction with (4), be solved efficiently (Zelt & Ellis 1988). Typical values of α between 0.025 and 0.1 result in a total traveltime error for ray paths through typical crustal models of less than ±0.002–0.01 s (Zelt & Ellis 1988). Within constant-velocity trapezoids, straight ray paths are used.

A ray traced through the model is defined only at a series of points, the number and spacing of which is dependent on the value of α. The traveltime at the endpoint of the ray is evaluated by numerical integration along the ray path using the trapezoidal rule.

3.2 Ray take-off angles

Rapid forward modelling is achieved by the ability to determine the take-off angles of particular ray groups using an iterative shooting/bisection technique (search mode) described in detail by Zelt & Ellis (1988). A ray group is defined as a set of rays that have all turning and/or reflection points in the same layer or layers. For a refracted (turning) ray group, the take-off angles of the shallowest and deepest ray to turn within a specified layer are determined using the iterative search mode and the complete ray group consists of those rays with take-off angles between the shallowest and deepest ray take-off angles (Fig. 3a). For a reflected ray group, the take-off angle of the ray that grazes off a specified layer boundary is determined using the same iterative technique and the complete ray group consists of those rays with take-off angles between the grazing-ray take-off angle and a specified angle as close to 90° as needed (Fig. 3b). For a head wave ray group, the take-off angle of the ray that intersects a specified layer boundary at the critical angle, within a specified tolerance, is determined and the complete ray group consists of rays that travel along the layer boundary and emerge upward at the critical angle (Fig. 3c). The initial take-off angles used in the search mode are calculated analytically assuming a laterally homogeneous model equivalent to that directly beneath the source (Zelt & Ellis 1988). The number of rays traced in the iterative search mode depends on the velocity model (i.e. velocity gradients and amount of lateral variation). Often fewer than 20 rays are required to determine a specific take-off angle, although more than 100 rays is not uncommon. Through extensive experimentation the search mode has been found to work efficiently for complex models with large lateral velocity variations (see Boland & Ellis 1989). If necessary, take-off angles can be supplied by the user.

To obtain multiple and/or free surface reflections, the refracted, reflected and head wave ray groups can be modified using a simple numerical code to include any number or combination of reflection points at any layer boundaries.

The iterative search mode is based on determining the minimum and maximum take-off angles of ray groups, as opposed to two-point ray tracing in which rays are traced to specific receiver locations. Therefore, the traveltime (and partial derivatives used in the inversion) associated with a specific receiver location is determined by linear interpolation across the endpoints of the two closest rays that bracket the point of interest. It is therefore necessary to extend the model slightly beyond the ends of the receiver array to ensure that these points can be bracketed by rays on either side. As the amount of lateral velocity variation increases within the model, it is necessary to trace more rays in each ray group to obtain sufficiently accurate interpolated traveltimes. This method of determining take-off angles is used since it is more robust and computationally less intensive than two-point ray tracing.

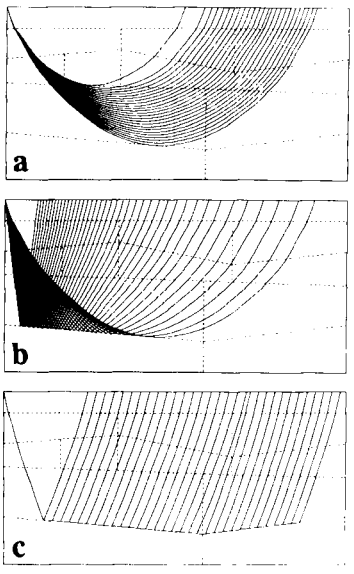

Figure 3. An example of the refracted (a), reflected (b), and head wave (c) ray groups for a single layer.

3.3 Smooth layer boundary simulation

Blocky model parametrizations, i.e. models with discontinuous changes in velocity or velocity gradient, have a tendency to scatter and focus ray paths when applied to infinite-frequency ray propagation, often causing geometrical shadow zones at the surface. This effect is undesirable since it is not characteristic of the wave propagation being modelled. An effective simulation of smooth layer boundaries can be applied in which the boundaries, consisting of connected linear segments, are uniformly sampled at many points, typically a few hundred, and smoothed by applying a three-point averaging filter. Ray tracing remains unaffected by the simulation except the incoming and outgoing angles at layer boundaries are determined using the slope of the smoothed boundary. This simulation can have a significant effect on ray paths that cross a layer boundary near a point where the original boundary consists of two line segments of differing slope (Fig. 4).

The general accuracy of the simulation can be increased by subdividing the original boundary into smaller linear

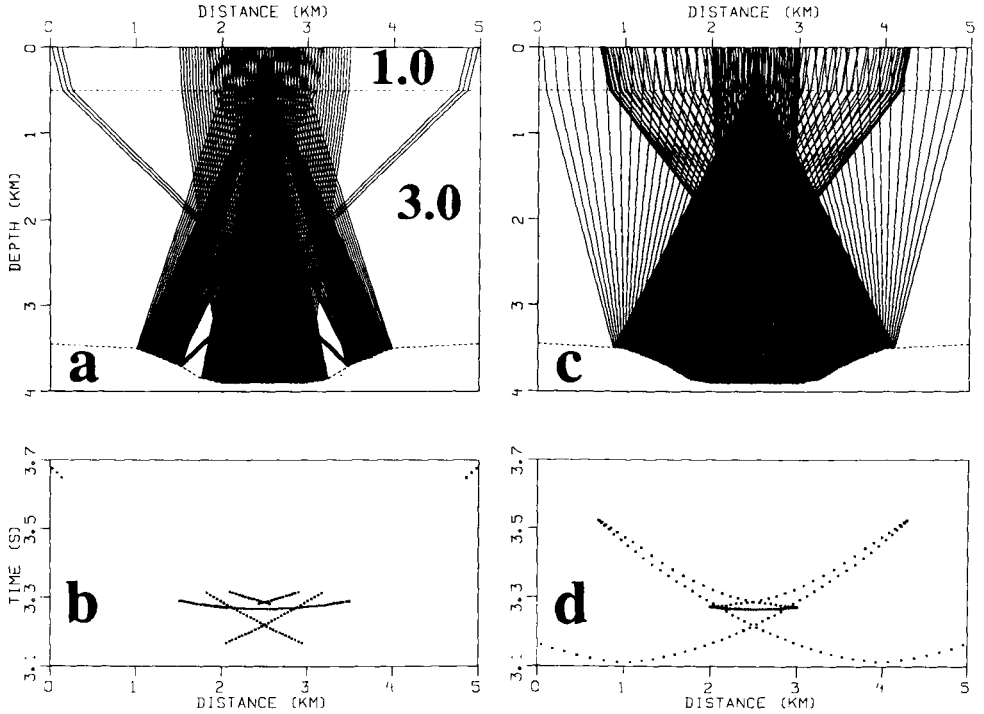

Figure 4. Example of the smooth layer boundary simulation. The same rays are traced through the same model in (a) and (c) (only rays reaching the surface are shown) and the corresponding traveltimes are shown in (b) and (d), respectively. The *P*-wave velocity in km s^{-1} is indicated for the upper two layers in (a). There is no vertical exaggeration of the models in (a) and (c). The smooth layer boundary simulation was applied to the synclinal interface in (c). Note the smoothed and extended traveltime curves in (d) as compared to those in (b).

segments near points with large changes in slope. Ray scattering and focusing and geometrical shadows caused by model 'blockiness' will be reduced and traveltime curves will be smoothed in accordance with the amount of boundary smoothing. The additional CPU time required for the smooth layer boundary simulation is less than 10 per cent. For models with boundaries having large lateral variations, the simulation yields more stable inversion results since it reduces or removes geometrical shadows and extends traveltime branches so that more observed data is used (Fig. 4).

4 INVERSION

The traveltime t between a source and receiver along a ray path L is given in integral form for a continuous velocity field $v(x, z)$ as

$$t = \int_L \frac{1}{v(x, z)}\, dl. \tag{5}$$

The discrete form

$$t = \sum_{i=1}^{n} \frac{l_i}{v_i}$$

is used in practical applications, where l_i and v_i are the path length and velocity of the ith ray segment, respectively. Therefore, traveltime is a linear combination of slowness (reciprocal of velocity), but traveltime inversion is a non-linear problem since the ray path is velocity dependent. The problem is solved by linearizing using a Taylor series expansion about a starting model and dropping higher order terms. As a consequence of this expansion, a starting model and iterative approach are necessary.

The linearized equation based on the assumption of neglecting higher-order terms is

$$\mathbf{A}\Delta\mathbf{m} = \Delta\mathbf{t} \tag{6}$$

where $\mathbf{A}$ is the partial derivative matrix, $\Delta\mathbf{m}$ is the model parameter adjustment vector, and $\Delta\mathbf{t}$ is the traveltime residual vector. The partial derivative matrix contains the elements $\partial t_i/\partial m_j$, where t_i is the ith observed traveltime and m_j is the jth model parameter selected for inversion, either a velocity value or the z coordinate of a boundary node. Both the traveltime residual vector and the partial derivative matrix are computed while ray tracing through a model during a particular iteration. The partial derivatives are calculated analytically, thus, no extra rays are traced to numerically approximate the derivatives by differencing. After ray tracing, the parameter adjustment vector is solved for in (6) and applied to the current model, after which rays are traced through the updated model. This procedure is repeated until a satisfactory fit to the observed data is achieved or a prescribed stopping criterion is satisfied. These are the steps of the basic inversion algorithm, first applied in this manner to traveltime inversion of crustal seismic data by Spence, Clowes & Ellis (1985).

4.1 Partial derivatives

The elements of the matrix of partial derivatives, $\mathbf{A}$, dimensioned $M \times N$ where M is the number of data and N is the number of model parameters, are calculated analytically during ray tracing for those model parameters selected for

adjustment, both velocities and boundary nodes simultaneously. From (5),

$$\frac{\partial t}{\partial v_j} = \int_L -\frac{1}{v^2}\frac{\partial v}{\partial v_j}\,dl$$

where v_j is the jth velocity value selected for inversion. The partial derivative within the integral can easily be evaluated using (1) and (2). The corresponding coefficients, like those in (2), are also pre-calculated prior to ray tracing. The partial derivatives associated with boundary nodes are derived through simple geometrical considerations, first presented by Spence (1984). Their derivation is provided in the Appendix to correct an error and introduce a modification necessary for stability.

4.2 Calculating traveltimes and partial derivatives at observed receiver locations

Each traveltime pick to be inverted is identified by a numerical code that indicates the phase of the arrival (i.e. refraction or reflection in a particular layer). The proper phase identification is the most important step made by the seismologist since the misidentification of a phase will cause unpredictable and potentially gross errors in the final model. Therefore, less obvious, later phases should not be included in the inversion until they can be positively identified through trial-and-error forward modelling.

Each ray group that is traced must also be identified with the same numerical code to allow for comparison of the calculated traveltimes with the appropriate observed traveltime picks. After each ray group is traced, the calculated traveltime and partial derivatives associated with a particular observed receiver location are determined by linear interpolation across the two closest ray endpoints. If an observed receiver location is bracketed by more than one pair of ray endpoints within a single ray group (e.g. a triplication), the calculated traveltime and partial derivatives are obtained from the pair of rays whose interpolated traveltime is a minimum. More than one ray group may be assigned the same code and the algorithm again determines the calculated traveltime and partial derivatives at the receiver location from the ray group that has the pair of rays with minimum interpolated traveltime. For example, refracted ray groups may be assigned the same code if the model has a sequence of layers with small or no velocity discontinuities between the layers, in which case it is generally not possible to know in advance in which layer the rays corresponding to the refracted arrivals will turn. The observed traveltime branches are not resampled at a uniform receiver spacing since this may cause an artificial increase or decrease in resolution of a particular region of the model.

4.3 Damped least-squares inversion

The inverse problem is generally overdetermined so (6) is solved using a damped least-squares technique (Aki & Richards 1980). The method used here is similar to that described by Lutter *et al.* (1990); therefore, only a brief summary and the associated calculation of resolution and uncertainty will be presented. The damped least-squares solution to (6) can be written as

$$\mathbf{\Delta m} = (\mathbf{A}^T\mathbf{C}_t^{-1}\mathbf{A} + D\mathbf{C}_m^{-1})^{-1}\mathbf{A}^T\mathbf{C}_t^{-1}\mathbf{\Delta t} \tag{7}$$

where $\mathbf{C}_t$ and $\mathbf{C}_m$ are the estimated data and model covariance matrices given by

$$\mathbf{C}_t = \text{diag}\,\{\sigma_i^2\}, \qquad \mathbf{C}_m = \text{diag}\,\{\sigma_j^2\},$$

and D is an overall damping parameter, usually equal to one (Menke 1984).

The standard deviation, σ_i, is the estimated uncertainty of the ith traveltime measurement. The value of σ_j is an *a priori* estimate of the uncertainty of the jth model parameter. For a particular solution of (7), a single value of $\sigma_j(\sigma_v)$, typically 0.1 km s^{-1}, was used for all velocities and a single value of $\sigma_j(\sigma_z)$, typically 0.1–1.0 km, was used for all boundary nodes. The relative values of σ_v and σ_z determine the trade-off between the size of velocity and boundary adjustments in the inversion. The value of D determines the overall trade-off between the resolution and uncertainty of model parameters as well as the size of parameter adjustments. Since the number of model parameters is generally much less than the number of observations, and the model is 2-D, the matrix to be inverted in (7) is relatively small and not particularly sparse. Therefore, the matrix inversion is performed using a simple LU (lower–upper) decomposition (Press *et al.* 1986).

The model resolution matrix is given by

$$\mathbf{R} = (\mathbf{A}^T\mathbf{C}_t^{-1}\mathbf{A} + D\mathbf{C}_m^{-1})^{-1}\mathbf{A}^T\mathbf{C}_t^{-1}\mathbf{A}. \tag{8}$$

The diagonal elements of the resolution matrix range between zero and one and indicate the degree of averaging or linear dependence of the true model as represented by the inverted model. Equivalently, they indicate the relative number of rays that sample each model parameter. Testing and experimentation with synthetic and real data has shown that model parameters associated with diagonal elements of the resolution matrix with values greater than 0.5 are generally well resolved and reliable, although in a few cases this arbitrary cut-off of satisfactory resolution is inappropriate, i.e. a velocity value constrained by many ray paths with a narrow angular distribution.

The *a posteriori* model covariance matrix is given by

$$\mathbf{C} = (\mathbf{I} - \mathbf{R})\mathbf{C}_m \tag{9}$$

where $\mathbf{I}$ is the identity matrix (Tarantola 1987). By taking the square root of the diagonal elements of $\mathbf{C}$, the calculated standard errors or uncertainties of the model parameters are obtained. These calculated errors are considered to represent a lower bound of the true parameter errors since they are due only to the uncertainties of the traveltime picks and fail to account for the trade-offs between model parameters, as well as other possible sources of error, such as: (1) phase misidentification; (2) modelling 3-D structure as 2-D; (3) assuming a straight line for the receiver geometry; (4) using an inappropriate model parametrization to represent the true earth (i.e. number of layers or number of velocity and boundary nodes); and (5) using a layered, large-block parametrization although the real earth is considerably more heterogeneous. Therefore, the calculated error estimates are best used in a relative rather than absolute sense.

4.4 Spatial resolution and absolute parameter uncertainty

An estimate of the spatial resolution of the final model centred about a specific velocity or boundary node can be obtained using the following test. First, select a single parameter of the final model and perturb its value on the order of its estimated uncertainty (σ_j). Second, trace rays through the perturbed model to calculate the associated traveltimes and interpolate these at the observed receiver locations assigning the observed pick uncertainties at each location. Finally, reset the value of the selected parameter to its value in the final model and invert the calculated data involving all model parameters that were determined at the same time as the selected parameter during the inversion for the final model. The spatial resolution about the selected parameter will be indicated by the amount that the values of adjacent parameters differ from the corresponding values in the final model. If the final model is well resolved about the selected parameter, then all other parameter values will be equal to the corresponding values in the final model. If the model is poorly resolved about the selected parameter, then the parameter's perturbation will be 'smeared' into adjacent parameters, perhaps both velocities and boundary depths if both parameter types were involved, and the extent of the smearing indicates the model's resolution. Note that the parameter perturbation should be large enough to yield a significant traveltime anomaly with respect to the picking uncertainties, but small enough to avoid significantly altering the ray path distribution.

To obtain an estimate of a parameter's absolute uncertainty, perturb its value from that in the final model and hold it fixed while inverting the observed data involving all other parameters that were determined at the same time as the perturbed parameter during the inversion for the final model. Then, increase the perturbation until the final model so obtained is unable to fit the observed data as well as the original final model according to (1) the ability to trace rays to all observations, and (2) the result of an F test comparing the χ^2 values of the two final models. The maximum perturbation of the parameter that allows a comparable fit to the observed data is an estimate of its absolute uncertainty.

Both positive and negative parameter perturbations should be used in both tests. To apply this type of error analysis to all velocity and boundary nodes could take longer than the time required to obtain the final model. However, it may be sufficient to test only one or two representative velocity and boundary nodes for each layer. Note that both tests may be used to study trade-offs between model parameters.

4.5 Model non-uniqueness

A measure of the non-uniqueness of the final model is given by the uncertainty estimate of each model parameter obtained from (9) or the method described above. However, this probably accounts for less than the total possible model non-uniqueness. A better measure of non-uniqueness can be qualitatively estimated using two tests: (1) for the same model parametrization (i.e. position of velocity and boundary nodes), different starting models are run and the final models that fit the data equally well are compared; and (2) starting models with different numbers of layers and/or number and position of velocity and boundary nodes are run and the final models are again compared. The range of final models that fit the observed data equally well will give an indication of model non-uniqueness. Although it is only possible to run a small number of the total possible starting models, a sense of the non-uniqueness can be obtained by selecting a few reasonable starting models. Further non-uniqueness can be assessed by varying the damping, using different *a priori* estimates of parameter uncertainties, or holding certain parameters fixed for some iterations.

4.6 Reducing the number of independent model parameters

Three features of the model parametrization increase the stability of the inversion algorithm by reducing the number of independent model parameters required to represent essentially the same velocity structure. First, a layer boundary can be forced to maintain a zero velocity discontinuity. This reduces the number of independent model parameters since the velocity at the top of the lower layer equals the velocity at the base of the upper layer. This feature is used (1) if there is no evidence in the data to suggest a velocity discontinuity across a boundary, or (2) to divide a single layer of the model into two or more layers, without associated velocity discontinuities but allowing a change in the vertical velocity gradient, if the data permit increased resolution (i.e. number of model parameters) in a particular layer.

The second feature is the ability to fix the vertical velocity gradient within a layer. In this case the same number and x coordinates of upper and lower layer velocity points is specified and the vertical gradient is held fixed at each of these x coordinates during the inversion (i.e. the lower layer velocities are not determined independently of the upper layer velocities). This feature is particularly useful for layers in which refracted arrivals are observed but there is insufficient turning ray penetration throughout the layer to constrain the velocity gradient or it may be used to fix the gradients based on values obtained from amplitude modelling of the data.

The last feature is similar to the second except the layer thickness, not the velocity gradient, is fixed. The same number and x coordinates of upper and lower layer boundary nodes is used and the layer thickness is held fixed at each of these x coordinates during the inversion. This feature may be used, for example, if there is evidence for a transition layer based on amplitude modelling, but there is insufficient constraint on its thickness provided by the traveltime data alone.

4.7 Stopping criteria and number of model parameters

Two final aspects of the inversion algorithm are the stopping criteria and the selection of the number of model parameters and node spacing. These considerations are interrelated and no single rule or simple criteria has been established. Instead, an empirical approach based on inverting observed seismic data has been developed that represents a major contribution to this study as a whole and will be discussed in detail with respect to the real data

example to follow. Briefly, the final model selected is that which (1) provides the desired trade-off between RMS (root-mean-square) traveltime residual and parameter resolution, and (2) allows rays to be traced to all observation points. In general, traveltime residuals can be reduced by adding more model parameters; however, overall parameter resolution is concurrently reduced. Thus the need to achieve an appropriate trade-off between these two measures.

Often it is not possible to trace rays to all observation points using a model obtained from an inversion. A common cause of this problem is that the model consists of too many parameters, so the data are unable to adequately constrain all model parameters, causing an unrealistic oscillation of the velocity values laterally within a layer or the shape of a layer boundary, and/or a velocity reversal with depth at certain locations in the model. These features cause rays to focus and scatter resulting in shadow zones at the surface. A final model must be rejected if it is not possible to trace rays to most observation points since the picks used in the inversion correspond to geometrical arrivals, i.e. the corresponding ray paths obey Snell's law. It is more important that this requirement be satisfied, rather than ensuring that the final model does not allow rays to be traced to receivers that do not contain the corresponding arival type in the observed data. In the former case, the model is necessarily incorrect, whereas in the latter case there are reasons why these arrivals may not be present or picked in the observed data: (1) the theoretical amplitudes associated with these rays may be very small; (2) other phases within the observed data may interfere destructively with these arrivals; and (3) ray amplitudes are large adjacent to a shadow zone whereas the true amplitudes are less.

5 TEST USING SYNTHETIC DATA

It was necessary to test the inversion algorithm with synthetic data typical of crustal seismic experiments to (1) ensure that it recovers the true model in an idealized case, (2) study its convergence behaviour and sensitivity to noise, (3) understand the effects of damping and the *a priori* estimates of parameter uncertainties, and (4) interpret the calculated resolution and uncertainty estimates.

The example presented here using synthetic data is intended to illustrate the algorithm's convergence behaviour and sensitivity to realistic noise levels as well as to provide a reference point for the parameter resolution estimates of the real data example to follow. The velocity model and traveltimes are representative of a typical wide-angle seismic crustal experiment. The true model is laterally heterogeneous and consists of three layers representing the upper and lower crust and upper mantle (Fig. 5, Table 1). The upper and lower velocity in each layer and the mid-crustal and crust–mantle (Moho) boundary are specified at 0, 100 and 200 km, for a total of 24 independent model parameters (18 velocity points and 6 boundary nodes).

Synthetic traveltimes for refracted and reflected phases were generated by tracing turning rays in each layer and reflected rays off the mid-crustal boundary and Moho from shot points at 0 and 200 km. Linear interpolation was used to obtain ray coverage at a receiver spacing of 5 km between 5 and 195 km, for a total of 39 seismograms and 240 arrivals. A second set of synthetic traveltimes was constructed by adding Gaussian noise to the arrival times with a standard deviation of ±0.05 s for refractions in the upper crust, ±0.1 s for refractions in the lower crust and upper mantle, and ±0.15 s for all reflections.

The starting velocity model used to invert both sets of data is laterally homogeneous and consists of the same number of layers and model parameters and the same node positions as the true model (Table 1). The velocities of the starting model are 0.1–1.1 km s^{-1} less than the corresponding true values and the boundary nodes are 1–6 km deeper. Since the position of all velocity and boundary nodes in the starting model are the same as the true model, any discrepancies between the final model obtained from the inversion of the data without added noise and the true model will illustrate the resolution limit of this experimental geometry and set of arrivals. A comparison between the final models obtained from the data with and without added noise will demonstrate the algorithm's sensitivity to a realistic level of random noise.

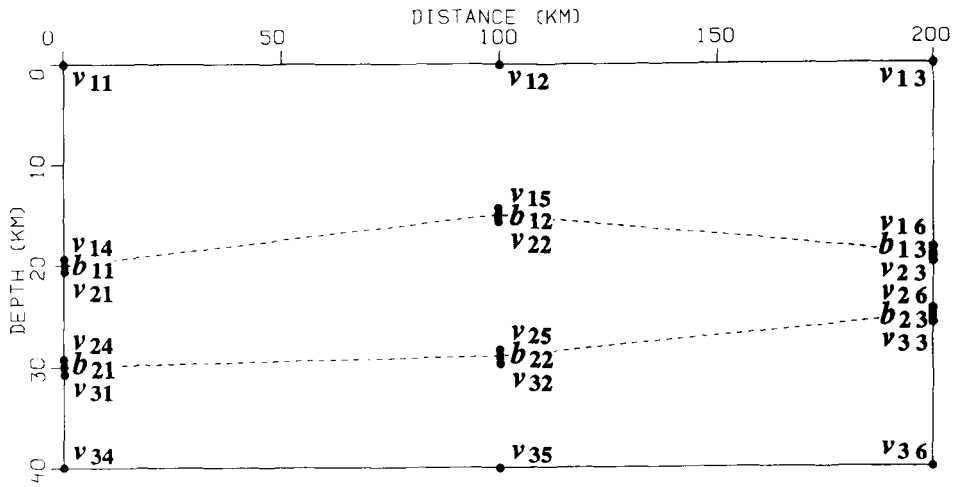

Figure 5. Parameters defining the true model of the synthetic test. The dashed lines are layer boundaries. The velocity and boundary nodes are labelled and indicated by circles and squares, respectively (see Table 1).

Table 1. Comparison of true and final models for the synthetic data with and without added noise. The parameter v_{ij} refers to the jth velocity point (km s^{-1}) in the ith layer (see Fig. 5). The parameter b_{ij} refers to the jth boundary node (km) at the base of the ith layer (see Fig. 5). R is the corresponding diagonal element of the resolution matrix given by (8). σ is the uncertainty estimate equal to the square root of the diagonal element of the covariance matrix given by (9).

			NOISE-FREE DATA			NOISY DATA		
PARAMETER	TRUE VALUE	STARTING VALUE	FINAL VALUE	R	σ	FINAL VALUE	R	σ
v_{11}	5.50	4.90	5.50	.999	.0038	5.47	.963	.0194
v_{12}	5.00	4.90	5.00	.996	.0065	5.03	.862	.0372
v_{13}	6.00	4.90	6.00	.998	.0041	5.97	.958	.0205
v_{14}	5.80	5.70	5.79	.982	.0133	5.84	.680	.0565
v_{15}	6.00	5.70	6.01	.995	.0070	6.02	.869	.0362
v_{16}	6.20	5.70	6.19	.981	.0138	6.22	.659	.0584
b_{11}	20.0	21.0	20.0	.999	.0262	20.0	.930	.2643
b_{12}	15.0	21.0	15.0	.990	.1019	15.9	.700	.5475
b_{13}	19.0	21.0	19.0	.999	.0269	18.8	.927	.2705
v_{21}	6.40	6.30	6.40	.967	.0181	6.32	.428	.0756
v_{22}	6.60	6.30	6.61	.988	.0111	6.75	.729	.0521
v_{23}	6.40	6.30	6.40	.961	.0198	6.55	.384	.0785
v_{24}	6.80	6.70	6.77	.858	.0376	6.82	.218	.0884
v_{25}	7.20	6.70	7.20	.984	.0127	7.09	.746	.0504
v_{26}	7.00	6.70	6.98	.911	.0298	6.85	.247	.0868
b_{21}	30.0	31.0	30.0	.998	.0441	30.6	.883	.3420
b_{22}	29.0	31.0	28.9	.977	.1503	27.3	.714	.5347
b_{23}	25.0	31.0	25.0	.998	.0443	25.5	.890	.3323
v_{31}	8.20	7.70	8.18	.883	.0343	8.01	.254	.0864
v_{32}	8.00	7.70	7.99	.985	.0121	7.92	.733	.0517
v_{33}	7.80	7.70	7.78	.906	.0307	7.72	.325	.0822
v_{34}	8.30	8.00	8.14	.195	.0897	8.08	.015	.0922
v_{35}	8.20	8.00	8.29	.720	.0529	8.45	.372	.0793
v_{36}	8.10	8.00	7.95	.206	.0891	8.06	.016	.0922

For the inversion of both sets of data, the following constants were used: $D = 1$, $\sigma_v = 0.1$ km s^{-1} and $\sigma_z = 1$ km. For the noise-free data, standard deviations of ± 0.01 s were used in the matrix $\mathbf{C}_t$ based on the maximum expected error of the synthetic traveltimes due to numerically solving the ray tracing equations and the interpolating used to obtain the traveltimes at a 5 km receiver spacing. For the data with added noise, the standard deviations in $\mathbf{C}_t$ were equal to the standard deviations of the Gaussian noise added.

Table 2 summarizes the results of the first three iterations of inverting the noise-free data. Note that the final model is obtained after three iterations as indicated by the χ^2 value of the third iteration. The RMS traveltime residual dropped from 1.92 to 0.004 s in three iterations and rays can be traced to 239 out of 240 arrivals using the final model. The final χ^2 value is considerably less than one since the errors of the synthetic traveltimes are on average less than the standard deviations used in the matrix $\mathbf{C}_t$. Table 3 summarizes the results of the first three iterations of inverting the data with added noise. The final model was obtained after only two iterations according to the χ^2 value. Rays can be traced to 238 out of 240 arrivals using the final model and the corresponding χ^2 value is 0.91. Figs 6 and 7 show the ray paths and the corresponding traveltime fit to the data with added noise for the starting and final models, respectively. A comparison between the true model and the final models obtained from inverting both data sets is given in Table 1. The calculated resolution and uncertainty estimates given by (8) and (9) are also indicated for each parameter of the final models. The average CPU time for one forward step and inversion was 12 and 3 s, respectively, on a SUN SPARCstation 1.

Table 2. Results of inverting noise-free synthetic data. Iteration zero refers to the starting model. N is the number of arrivals that can be bracketed by rays. T_{RMS} is the RMS traveltime residual with respect to the true synthetic data and χ^2 is the corresponding chi-squared value. The model obtained after three iterations is considered the final model according to the χ^2 value.

ITERATION	N	T_{RMS} (s)	χ^2
0	239	1.92	36973
1	233	0.16	259
2	237	.024	5.82
3	239	.004	0.17

Table 3. Results of inverting noisy synthetic data. See Table 1 for details. The model obtained after two iterations is considered the final model according to the χ^2 value.

ITERATION	N	T_{RMS} (s)	χ^2
0	239	1.92	396
1	237	0.18	3.07
2	238	0.11	0.91
3	239	0.11	0.90

For the final model obtained from the noise-free data, the velocities and boundary depths agree closely with the true model, except for the lower layer velocities in the upper mantle, the maximum differences being 0.03 km s^{-1} and 0.1 km, respectively. The lower layer velocities in the upper mantle differ by as much as 0.16 km s^{-1} due to the relatively

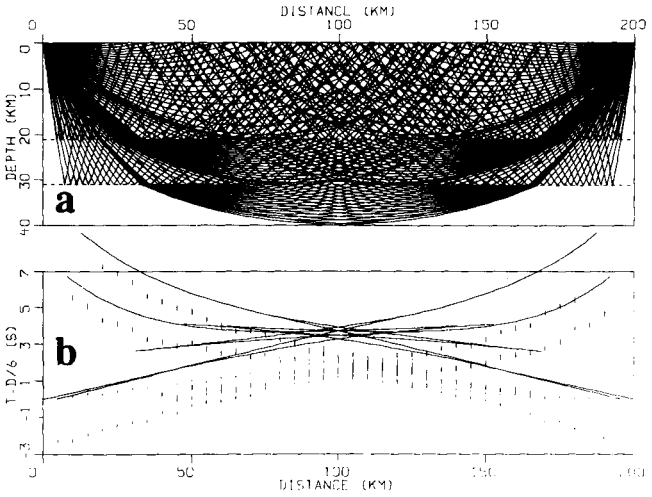

Figure 6. Ray path diagram (a) and traveltime comparison (b) for the starting model and the synthetic data with added noise. For clarity, every other ray used is shown in (a). The true synthetic data in (b) are indicated by vertical bars, the height of which equals twice the standard deviation of the Gaussian noise added to the data. The traveltimes associated with the rays traced in (a) are indicated by curves. A reducing velocity of 6 km s^{-1} has been applied.

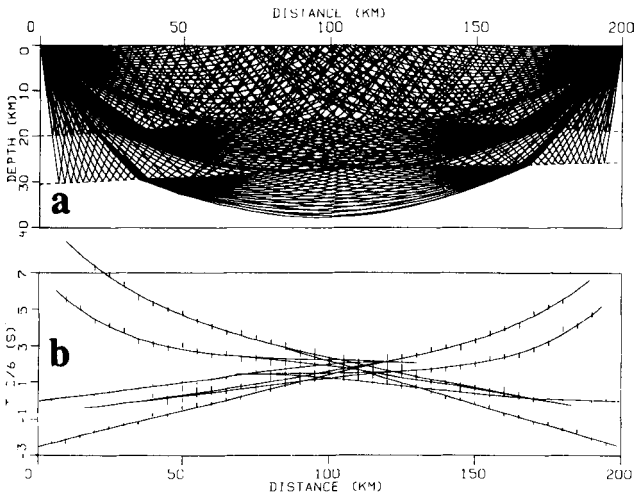

Figure 7. Ray path diagram (a) and traveltime comparison (b) for the final model after inverting the synthetic data with added noise. See Fig. 6 for details.

low ray coverage near these points as seen in Fig. 7(a) and indicated by their relatively low resolution and high uncertainty.

For the final model obtained from the data with added noise, the velocities and boundary depths also agree well with the true model but generally exhibit greater error than the model obtained from the noise-free data. The corresponding resolution and error estimates are also lower and higher, respectively, by as much as a factor of 10 for a few of the parameters. The resolution of the velocities at 0 and 200 km in the lower crust and upper mantle and the lower velocity at 100 km in the upper mantle are all less than 0.5 due to the relatively low ray coverage near the edges of the model. However, the final model has not been greatly affected by the added noise since for those velocities with a corresponding resolution greater than 0.5, the largest error with respect to the true model is 0.15 km s^{-1}. All boundary nodes have a corresponding resolution greater than 0.7 with a maximum difference with respect to the true model of 1.7 km.

Four additional inversions of the data with and without added noise were also performed in which all model parameters were overestimated and underestimated. This reduced the initial RMS traveltime residual to less than 1 s in each case since the effect on total traveltime of overestimating or underestimating both velocities and boundary depths trades off. The final models were obtained after three to six iterations and contained differences with respect to the true model comparable to those listed in Table 1. These tests show that it is possible for the inversion algorithm to resolve trade-offs between velocity and boundary depth. Note that more iterations were required in some cases due to the differences in ray coverage, and thus parameter resolution, for the starting models.

6 APPLICATION TO THE 1986 IRIS–PASSCAL NEVADA DATA

An application of the inversion method was made to the crustal seismic data acquired along the 200 km north–south profile of the 1986 IRIS–PASSCAL (Incorporated Research Institutions for Seismology-Program for Array Seismic Studies of the Continental Lithosphere) Basin and Range experiment in northwest Nevada (PASSCAL working group 1988). Five buried shots ranging in size from 900 to 1360 kg were recorded along the profile by an array of 120 vertical component recorders, providing an average receiver spacing of 1.7 km. A total of 683 P-wave arrivals and estimated picking errors were determined by Braun & Smith (1989) and used in the inversion, corresponding to 356 refracted rays through the upper crust (P_g), 109 reflections off a mid-crustal boundary (P_cP), 135 reflections off the crust–mantle boundary (P_mP), and 83 refracted rays or head waves through the upper mantle (P_n). The shot points, numbered 11, 10, 4, 9 and 8 from south to north, are located at 0, 46, 95, 136 and 197 km, respectively (Fig. 8). Fig. 8 shows an example of the quality of data from which the traveltimes were picked. The uncertainties of the traveltime picks used in the matrix $\mathbf{C}_t$ average ± 0.04 s (ranging between ± 0.03 and 0.08 s) for P_g and P_n, and average ± 0.17 and ± 0.14 s (ranging between ± 0.08 and 0.23 s) for P_cP and P_mP, respectively (Braun & Smith 1989).

These data are ideally suited to the inversion algorithm since (1) the number of shots and receivers allows relatively detailed velocity structure to be resolved, (2) the PASSCAL data quality is good and both refracted and wide-angle reflected crustal and upper mantle arrivals are uniformly distributed in all record sections, (3) previous 1-D traveltime and amplitude modelling of the end shots provides a suitable starting model and constrains the vertical velocity gradient in a few layers and the nature of the crust–mantle transition layer where the traveltime data alone cannot, and (4) other 1-D and 2-D interpretations of the data through forward and inverse modelling allow for a comparison of results. The main purpose of this example is to demonstrate the effectiveness of our inversion method to obtain 2-D velocity structure; the tectonic implications of the final velocity model will not be discussed here, but is emphasized by Benz, Smith & Mooney (1990) and Holbrook (1990).

The inversion of the Nevada PASSCAL data was performed in three successive steps: (1) inversion of the P_g arrivals for upper crustal structure to about 10 km depth; (2) inversion of the P_cP arrivals to define a mid-crustal boundary and the mid-crustal velocity above it; and (3) inversion of the P_mP and P_n arrivals simultaneously to determine the crust–mantle boundary and the velocity in the lower crust and upper mantle. This 'layer-stripping' procedure was used to simplify and speed up the inversion and is valid since tests showed that the P_cP arrivals provide no constraint on upper crustal structure and the P_mP and P_n arrivals provide no constraint on upper and middle crustal structure. A 1-D starting model (Table 4) was used at the beginning of each step based on an average of the two 1-D models obtained from the traveltime and amplitude modelling of data from shots 11 and 8 by Benz *et al.* (1990) using the 1-D reflectivity method. Although it would be straightforward to obtain the best-fitting 1-D model for the entire data set using the inversion algorithm and use it as the starting model, the P-wave velocity model of Benz *et al.* (1990) was used since it is further constrained by amplitude modelling and thus provides reliable estimates of velocity gradients and the nature of the crust–mantle transition

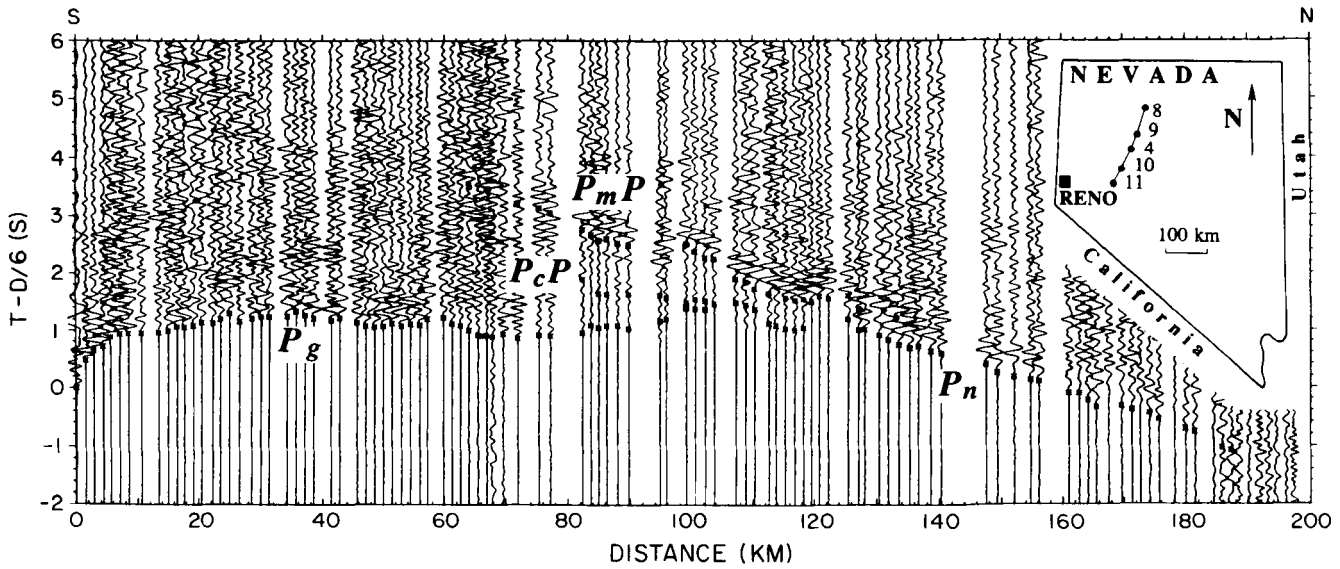

Figure 8. Seismic data for shot point 11 of the north–south line of the 1986 Nevada PASSCAL experiment. The traces have been scaled to a common maximum amplitude and a reducing velocity of 6 km s^{-1} has been applied. The picks of each phase used in the inversion are indicated by symbols; the four phases are labelled and described in the text. The inset shows the location of north–south PASSCAL line and the five shot points in northwest Nevada.

layer. The 2-D structure determined in steps (1) and (2) was held fixed during steps (2) and (3).

No corrections to the traveltime data were necessary to account for the variations in surface topography or near-surface velocity. Instead, the topography was sampled at 29 points and incorporated as the top layer boundary of the model. A non-uniform spacing was used to accurately represent the topography with as few points as possible. The maximum relief along the profile is 0.66 km with an average elevation of 1.3 km above sea-level. Depths within the model are given with respect to sea-level, positive values below sea-level. Large variations in near-surface velocity are apparent from the data and the mapped surface geology. These variations were grossly imaged by inverting the P_g arrivals; no additional surface information was incorporated into the model.

Table 4. Starting *P*-wave velocity model used to invert the north–south Nevada PASSCAL data. The velocity model is laterally homogeneous except for the surface relief that is represented by 29 points. The upper crust is represented by three layers. The depths are measured positive downward with respect to sea level. The upper and lower layer velocities are given for each layer except a constant velocity was used in the upper mantle.

LAYER	DEPTH (km)	*P*-WAVE VELOCITY (km/s)
	-1.3 (average)	
1 - upper crust		2.9-3.5
	0.25	
2 - upper crust		5.45-5.95
	4.2	
3 - upper crust		5.95-6.05
	8.2	
4 - middle crust		6.05-6.25
	17.0	
5 - lower crust		6.35-6.85
	33.2	
6 - upper mantle		7.9

The smooth layer boundary simulation was applied for all iterations. The value of D in (7) was 1.0 for all iterations except for a few in which it was increased as discussed below. The value of σ_v was 0.1 km s^{-1} for all velocities and the value of σ_z was 0.1 km for a shallow upper crustal boundary and 1.0 km for the mid-crustal boundary and the Moho.

One final comment regarding methodology is needed before presenting the detailed inversion of the PASSCAL data. The inversion algorithm is intended for crustal seismic data with a relatively low shot–receiver density with respect to the requirements of conventional tomographic or full wavefield techniques, i.e. the wavefield is spatially aliased. Since this type of crustal refraction/wide-angle reflection data can typically resolve relatively few model parameters, the model is intentionally underparametrized (fewer parameters than data) to make the ray tracing and inversion stable. To obtain the best possible final model, we found it necessary to determine the optimum number and location of velocity and boundary nodes that provide the desired trade-off between traveltime fit and parameter resolution, as well as the ability to trace rays to all observations. This step is what most strongly separates this method of inversion from algorithms that are applied to higher resolution data: the model cannot be parametrized in terms of a uniform grid of velocity nodes, the spacing of which is determined by the wavelength of the data. If this were attempted with data such as those obtained from the Nevada PASSCAL experiment, model smoothing and/or a set of empirical rules restricting parameter adjustment at each iteration would be necessary since the data cannot resolve such fine structure. To avoid this problem, the approach taken here is to underparametrize the model and run a series of inversions to determine the optimal number and position of velocity and boundary nodes that best match the data's subsurface resolution. Note that underparametrizing makes the inverse solution more dependent on the chosen model parametriza-

tion but stabilizes the inversion by removing the underdeterminancy of the problem.

6.1 Upper crust

The modelling of the 356 P_g arrivals began by assigning a velocity point at the surface at each of the five shot point locations and inverting the near-offset arrivals around each shot by fixing the near-surface vertical velocity gradient according to the velocity model of Benz *et al.* (1990). These arrivals are within 5–10 km of the shot points and have apparent velocities between 2.5 and 6.0 km s^{-1}. A layer boundary at 0.25 km depth with nodes at the five shot point locations was then added to the model along with two layers below this, each layer having upper and lower layer velocity points at the shot point locations. The interface separating these layers at 4.2 km depth has no velocity discontinuity but is intended to allow a change in the vertical velocity gradient as suggested by the amplitude modelling of Benz *et al.* (1990). An inversion of all P_g arrivals was then made by tracing refracted rays through each of the three layers of the model. The vertical velocity gradient in the first and third layers was fixed due to inadequate ray coverage within these layers to allow independent determination of the upper and lower layer velocities: in the first layer, turning rays occur only within about 10 km of each shot point, and in the third layer, all ray paths propagate nearly horizontally.

This upper crustal model has 20 independent parameters, 15 velocity points and five boundary nodes. After convergence, all parameters had good resolution (greater than 0.5) and rays were traced to all observations, however, the traveltime fit is relatively poor ($\chi^2 > 15$). Therefore, additional parameters (velocity and boundary nodes) were added to the model by placing a node between each pair of existing parameters, using the average of the two adjacent parameters as a starting value. This model has 36 independent parameters, 27 velocity points and nine boundary nodes. After convergence, only six parameters have a corresponding resolution less than 0.5, rays can be traced to all observations, and the traveltime fit is improved ($\chi^2 = 12.9$).

Adding more parameters did not significantly improve the traveltime fit and parameter resolution dropped sharply. In addition, large lateral velocity variations and a few velocity reversals with depth made it impossible to trace rays to all observations. Thus, the 36 node model was chosen as the final upper crustal model (Fig. 9). It extends to a depth of 7.8 km since this corresponds to the deepest turning point of a P_g ray path. Table 5 summarizes the results of inverting P_g. Note that the RMS traveltime residual was reduced from 0.39 for the starting model to 0.12 s for the final model.

During the inversion of the P_g arrivals, some of the idiosyncrasies of the inversion process became apparent. It was necessary to hold a few velocity values fixed during some iterations since they became unrealistically large or caused a velocity reversal with depth if they were allowed to vary and thus prevented rays from being traced to all observation points. No velocities were fixed for all iterations and some could be varied after having been fixed during previous iterations. In addition, in some locations, the vertical velocity gradient in the first and third layers was reduced to avoid unrealistically high velocities (greater than 6.4 km s^{-1}) at upper crustal depths. To obtain the best possible traveltime fit, it was necessary to increase the damping parameter, D, in (7) for some iterations. Its normal value is 1.0, but it was increased to as much as 100 in some cases to avoid obtaining an updated model with a significantly poorer traveltime fit. Note that the final parameter resolution estimates are calculated with $D = 1$ since it was used for most iterations and for consistency with the subsequent inversion of P_cP, P_mP and P_n.

The final upper crustal model has an associated χ^2 significantly greater than one. This is because the final model is underparametrized since the data cannot resolve

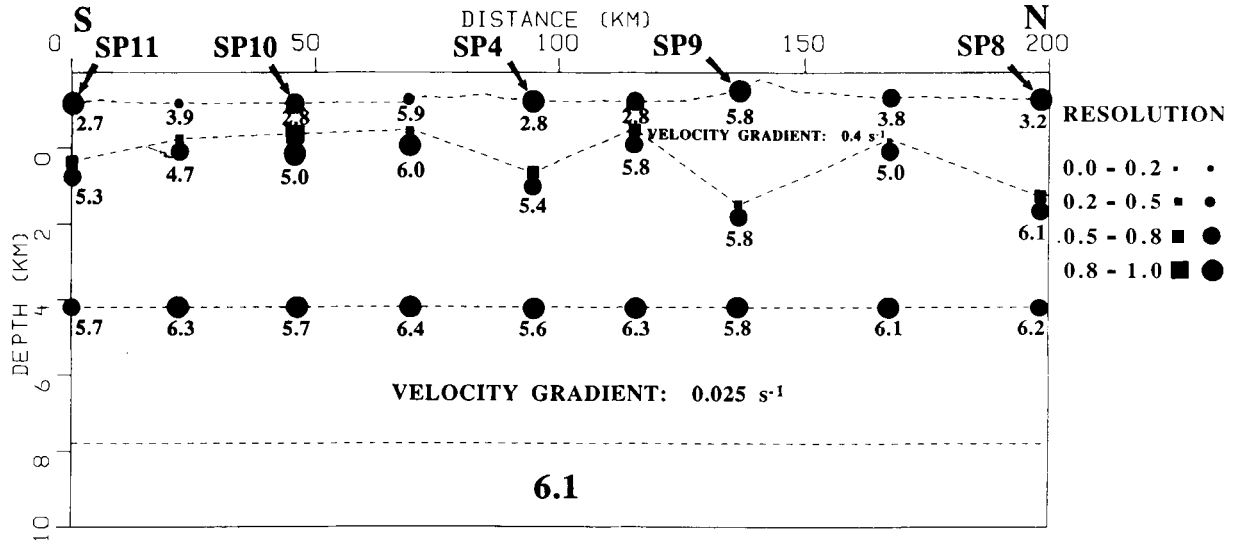

Figure 9. Final upper crustal *P*-wave velocity model for the north–south Nevada PASSCAL data. The five shot point locations are indicated. The dashed lines are layer boundaries. The velocity points are labelled in km s^{-1} and indicated by circles; the boundary nodes are indicated by squares. The size of the velocity and boundary nodes indicates their resolution given by (8). There is no velocity discontinuity across the boundary at 4.2 km depth. The vertical velocity gradient was fixed in the first and third layers according to the values indicated. The boundary at 7.8 km depth separates the upper and middle crust.

Table 5. Results of inverting the north–south Nevada PASSCAL data. N is the number of observations of a particular phase; rays were traced to all observations in the final model. $\bar{\sigma}_t$ is the average pick uncertainty. T_{RMS} is the RMS traveltime residual with respect to the observed data and χ^2 is the corresponding chi-squared value; the initial traveltime residual and χ^2 values for P_cP, P_mP and P_n were calculated after shallower phases were inverted. The number of model parameters constrained by each phase is indicated; N_v for velocity points and N_z for boundary nodes; the Moho boundary is constrained by P_mP and P_n. The CPU time for the forward step, T_f, and inversion, T_i, is determined on a SUN SPARCstation 1; a forward step involves ray tracing and calculating traveltimes and partial derivatives; and inversion involves solving (7); P_mP and P_n were inverted simultaneously.

			INITIAL		FINAL		PARAMETERS		CPU TIME (s)	
PHASE	N	$\bar{\sigma}_t$ (s)	T_{RMS} (s)	χ^2	T_{RMS} (s)	χ^2	N_v	N_z	T_f	T_i
P_g	356	0.04	0.39	141	0.12	12.9	27	9	86	6
P_cP	109	0.17	0.23	1.9	0.18	1.2	1	7	18	1
P_mP	135	0.14	0.28	4.1	0.18	1.6	1			
								} 10	26	1
P_n	83	0.04	0.26	41.6	0.10	6.3	1			

the small-scale heterogeneities that cause the rapid oscillation of the P_g traveltime branches. This is an important observation: if the data quality is high so that the uncertainties of the traveltime picks are small, it will not be possible to obtain a model with $\chi^2 = 1$ if the data have sampled small-scale heterogeneities that it cannot resolve. For example, consider a single-shot experiment over a region with many small-scale heterogeneities yielding high signal-to-noise data. It is clear that in this extreme situation, it would be impossible to achieve a well-resolved model with $\chi^2 = 1$. Therefore, we choose an underparametrized final model that provides the best trade-off between the RMS traveltime residual and parameter resolution and also allows rays to be traced to all the observations, not according to achieving $\chi^2 = 1$. Other factors that may contribute to a final χ^2 value greater than one are (1) significant out-of-plane structural and velocity variations, (2) deviations of the shot–receiver geometry from a straight line, and (3) some of the picks identified as P_g arrivals were non-geometrical arrivals (i.e. they were diffractions associated with a shadow zone or low-velocity body).

6.2 Middle crust

To invert the mid-crustal reflections, P_cP, the upper crustal model obtained from inverting P_g was held fixed. The 109 P_cP arrivals were used to determine the shape of the mid-crustal boundary as well as the mid-crustal velocity structure above it. A single layer was used to represent the middle crust and the vertical velocity gradient determined by Benz *et al.* (1990) was held fixed. The initial model of the middle crust and the vertical velocity gradient determined by Benz *et al.* (1990) was held fixed. The initial model of the middle crust comprised a single velocity point and boundary node, after which progressively more boundary nodes were added to lower the traveltime residual. The boundary nodes were evenly spaced between 25 and 175 km. After convergence using a model with a particular number of boundary nodes, the subsequent starting model, with one additional node, had a boundary shape that was as close as possible to its shape in the previous final model with one less boundary node. This procedure of adding boundary nodes was continued until it was no longer possible to trace rays to all observations because of a large oscillation in the boundary shape.

The final mid-crustal model has seven boundary nodes with a 25 km spacing (Fig. 10). The five inner nodes have resolution values greater than 0.65 and $\chi^2 = 1.2$ (Table 5). Possible causes of the large boundary oscillations that result if greater than seven nodes are used are (1) the mid-crustal boundary is not piece-wise continuous as modelled, but is discontinuously offset, such as by faulting, (2) the picked P_cP phases do not correspond to reflections off the same boundary for each shot, (3) the inversion is unstable because of relatively large errors in the P_cP picks, or (4) there is a

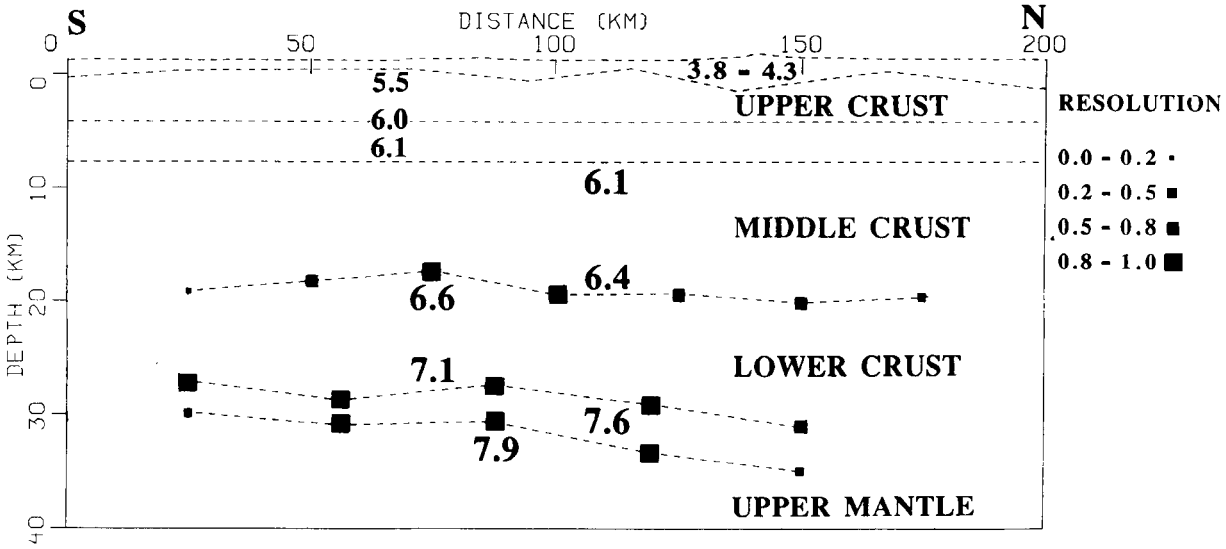

Figure 10. Final P-wave velocity model for the north–south Nevada PASSCAL data. The dashed lines are layer boundaries. The average upper and lower layer velocities of the three upper crustal layers are indicated; the detailed structure is presented in Fig. 9. The upper and lower layer velocities of the middle and lower crust and the upper mantle velocity are indicated in km s^{-1}. The nodes defining the mid-crustal boundary and the Moho are indicated by squares, the size of which indicates their resolution given by (8).

trade-off between velocity and boundary depth not constrained by the data. An attempt was made to reduce the value of χ^2 by using multiple velocity points in the mid-crustal layer, i.e. allowing lateral velocity variations. This did not significantly lower the value of χ^2 and the velocity tended to oscillate unrealistically across the layer.

The inability to resolve the detailed mid-crustal velocity structure using reflected arrivals was not unexpected given the relatively large uncertainties of the P_cP picks and the absence of picks at wide-angle offsets. The high resolution of the single mid-crustal velocity value (0.949) is a result of the large number of P_cP ray paths constraining a single velocity value. However, tests showed that the mid-crustal reflections could be fit equally well using a range of upper layer velocities between 5.9 and 6.4 km s^{-1} because all P_cP arrivals correspond to ray paths with similar, relatively steep directions of propagation.

6.3 Lower crust and upper mantle

The 218 P_mP and P_n arrivals from the lower crust and upper mantle were inverted simultaneously because they both constrain the crust–mantle boundary. In addition, the P_mP phase provides the primary constraint on the lower crustal velocity between the mid-crust and the Moho, and the P_n phase constrains the upper mantle velocity. For the inversion of P_mP and P_n, the final upper and mid-crustal models obtained from inverting P_g and P_cP were held fixed. Single layers were used to represent the lower crust and upper mantle. The vertical velocity gradient in the lower crust was fixed according to the 1-D reflectivity modelling of Benz *et al.* (1990) and a constant velocity was used in the upper mantle layer since head waves were used to model the P_n arrivals and turning ray propagation was not required. The initial model for the lower crust/upper mantle comprised a single velocity point in each layer and a single boundary node. The same procedure of adding boundary nodes to invert the P_cP arrivals was applied to the Moho, except the nodes were evenly spaced between 25 and 150 km due to the asymmetry of the subsurface P_mP and P_n ray coverage.

The final model, using a velocity discontinuity to represent the Moho, consists of five nodes with a 31.25 km spacing. The resolution of each node is greater than 0.85 and $\chi^2 = 1.8$ and 8.0 for the P_mP and P_n arrivals, respectively. It was found that the shape of the crust–mantle boundary was unrealistically oscillatory if more than five boundary nodes were used and a significant improvement to the fit of the data was not obtained by allowing a lateral velocity variation in either the lower crust or upper mantle. The latter result is primarily due to a lack of resolution caused by the similar propagation directions of the P_mP and P_n ray paths in the lower crust and upper mantle, respectively.

The amplitude modelling of P_mP and P_n by Benz *et al.* (1990) suggests that the Moho does not represent a velocity discontinuity, but is rather a transition zone a few kilometres thick, i.e. the boundary at which most energy is reflected may not correspond to the boundary beneath which the P_n rays propagate. This is weakly suggested by the traveltime data and may partially explain the relatively high value of χ^2 for the P_mP and P_n phases and the low upper mantle velocity (7.7 km s^{-1}).

To improve the fit to the P_mP and P_n arrivals, a transition layer was incorporated into the model. The initial thickness of this layer was obtained from the Benz *et al.* (1990) model: an additional boundary node was positioned 3 km below each of the five nodes in the final model obtained using a velocity discontinuity to represent the Moho. Since in the forward modelling, rays are reflected off the top (P_mP) and head waves propagate along the bottom (P_n) of the transition layer, the velocity within the transition zone is not constrained by the traveltime data and was therefore fixed at 7.6 km s^{-1} according to the Benz *et al.* (1990) model.

Since the traveltime data only weakly constrain the transition layer thickness, large damping ($D = 100$) was used to obtain the final model after a few iterations. The thickness of the transition layer varies between 2.2 and 4.2 km at the five node locations and the upper mantle velocity increases to 7.9 km s^{-1} as compared to 7.7 km s^{-1} if a transition layer is not used (Fig. 10). The top of the transition layer is similar to the boundary obtained if a velocity discontinuity is used to represent the Moho. The resolution of the 10 boundary nodes is each greater than 0.75 except the nodes at 25 and 150 km of the lower layer boundary which have resolutions slightly less than 0.5. The final value of χ^2 is 1.6 and 6.3 for the P_mP and P_n arrivals, respectively (Table 5).

The ray path diagram and comparison between the observed and calculated traveltimes for shot 11 and the P_mP phase for all shots using the complete final model are shown in Figs 11 and 12, respectively. The ray diagrams indicate the ray coverage associated with each phase. The traveltime comparisons show that the general trends of the observed phases are matched by the final model. However, they also illustrate that the rapid oscillations of the observed traveltime branches were not well matched by the

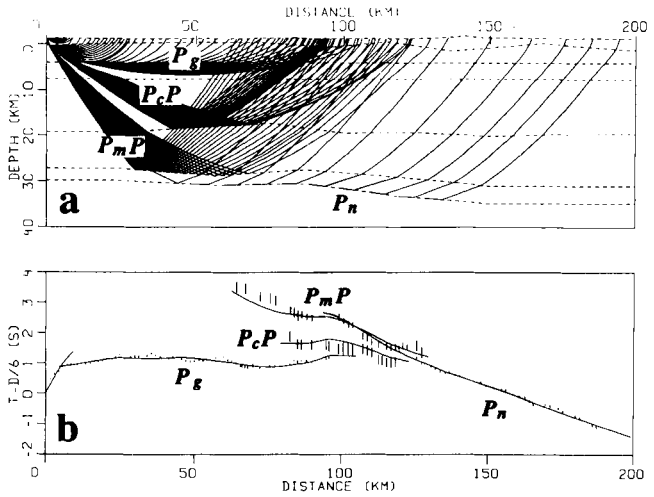

Figure 11. Ray path diagram (a) and traveltime comparison (b) for shot point 11 using the final model for the north–south Nevada PASSCAL data. The four phases are labelled in (a) and (b). For clarity, every other ray used is shown in (a). The observed data in (b) are indicated by vertical bars, the height of which equals twice the uncertainty of the pick. The traveltimes associated with the rays traced in (a) are indicated by curves.

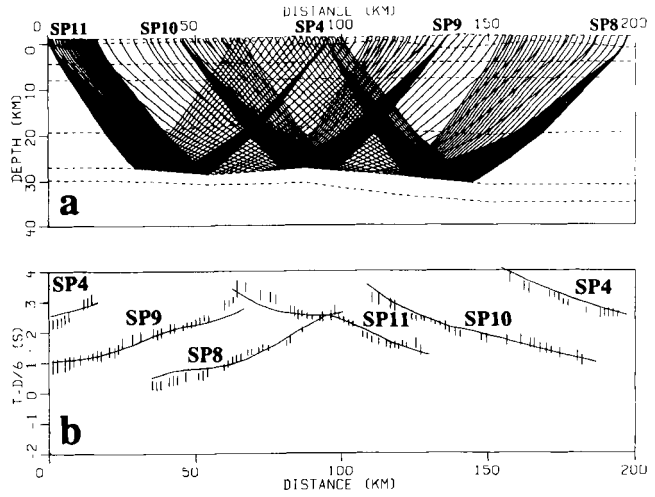

Figure 12. Ray path diagram (a) and traveltime comparison (b) for the P_mP phase using the final model for the north–south Nevada PASSCAL data. The five shot points are labelled in (a) and the corresponding arrivals are labelled in (b). See Fig. 11 for details.

theoretical values and resulted in χ^2 values of significantly greater than one.

6.4 Comparison with velocity models from other studies

This section presents a comparison of the final *P*-wave velocity model for the north–south line of the 1986 Nevada PASSCAL seismic experiment obtained from this inversion study with models obtained from four other studies using the same seismic data, but different 1-D and 2-D methods of forward and inverse modelling. The purpose of comparing the general features of the final models is twofold. First, the comparisons serve as a check on the validity of our inversion technique. Note that when comparing final models, it is necessary to be aware of the inherent limitations of a particular interpretational technique, i.e. a 1-D as compared to 2-D analysis, or techniques that make use of different types and/or amounts of information contained in the data, i.e. amplitude modelling. The second purpose of these comparisons is to provide a more realistic estimate of the absolute parameter uncertainties than is given by (9). The differences between comparable features in the final models will yield an uncertainty estimate that accounts for the bias introduced by the interpreter, i.e. phase identification and picking, as well as the bias associated with a particular modelling approach, i.e. model parametrization. For consistency with other seismic studies of the 1986 Nevada PASSCAL data, the model depths from this study are referred to the average surface elevation, 1.3 km above sea-level.

The average 1-D velocity structure obtained from our 2-D model is very similar to the average of the two 1-D models of shot points 11 and 8 obtained by Benz *et al.* (1990) using the reflectivity method. The only major differences are:(1) the average velocity at the surface increases from 3.8 to 4.3 km s^{-1} in the first layer of our model and increases from 2.9 to 3.5 km s^{-1} in the Benz *et al.* (1990) model; and (2) the lower crustal velocity increases from 6.6 to 7.1 km s^{-1} in our model and increases from 6.4 to 6.9 km s^{-1} in the Benz *et al.* (1990) model. The former difference is not unexpected given the larger lateral variations in the near-surface. The latter difference may be due to the poor constraint of the lower crustal velocity provided by the traveltime data since no arrivals corresponding to turning rays in this layer were used in the inversion. The average Moho depth and upper mantle velocity is 32.5 km and 7.9 km s^{-1} in our model, respectively, as compared to 34.5 km and 7.9 km s^{-1} in the 1-D model of Benz *et al.* (1990).

Hawman *et al.* (1990) used a τ–p inversion method to derive a 1-D velocity model for each shot of the 1986 experiment. They obtained an average crustal velocity of 6.2 km s^{-1} as compared to 6.25 km s^{-1} for our model and estimated the velocity near the base of the crust to be 7.4 km s^{-1}. This agrees well with the average of the velocity at the base of the crust (7.1 km s^{-1}) and the velocity of the crust–mantle transition layer (7.6 km s^{-1}) in our model. Hawman *et al.* (1990) suggest an average crustal thickness of 30.5 km as compared with 32.5 km in our model.

The same traveltime picks and corresponding uncertainties used in this study were also inverted by Braun & Smith (1989) using the 2-D ray trace/inversion method of Lutter *et al.* (1990) and Lutter & Nowack (1990). However, Braun & Smith (1989) resampled the traveltime branches at a uniform receiver spacing and used a different weighting scheme based on the uncertainties of the picks. Surface relief was not incorporated into their model and they did not use the P_n phase, hence the Moho was only constrained by the P_mP phase. Also, a 1-D velocity field obtained from the Benz *et al.* (1990) modelling was used below 6 km depth and held fixed during the inversion for the mid-crustal boundary and the Moho.

The near-surface velocity variations in the Braun & Smith (1989) model are similar to ours, varying over 3 km s^{-1}. However, the average velocity at any depth throughout their model is consistently 0.1–0.3 km s^{-1} less than in our model. This is probably because (1) the vertical velocity gradients were not well constrained in the upper crust of the Braun & Smith (1989) model, and (2) in the middle and lower crust, the velocity structure was not determined as part of the inversion, but was held fixed. The shapes of the mid-crustal boundary and the top of the crust–mantle transition zone are similar to ours, except they are about 2 km shallower due to the consistently lower velocities throughout the Braun & Smith (1989) model. The RMS traveltime residuals of the P_g, P_cP and P_mP phases are 0.12, 0.18 and 0.16 s, respectively, as compared to 0.12, 0.18 and 0.18 s for our model. The larger residual associated with the P_mP phase for our model is probably a result of inverting P_mP and P_n simultaneously in which the P_n picks have smaller uncertainties and thus are more highly weighted in the inversion.

Holbrook (1990) obtained a 2-D model through conventional trail-and-error ray-trace forward modelling of traveltimes and amplitudes. It contains similar large lateral *P*-wave velocity variations in the upper few kilometres and a basement velocity that ranges from 5.4 to 5.9 km s^{-1}, compared to 4.7 to 6.1 km s^{-1} in our model. The mid-crustal velocity increases from 6.0 to 6.2 km s^{-1}, less than our 6.1 to 6.4 km s^{-1} increase. Holbrook's (1990) model also contains a localized low-velocity body (5.5 km s^{-1}) in the mid-crust between 30 and 100 km that we could not discern

since arrivals corresponding to reflections off this body were not identified by Braun & Smith (1989).

The average depth of the mid-crustal boundary is the same as in our model, 20.5 km, although the boundary shapes are quite different. The velocity in the lower crust of the Holbrook (1990) model is 6.6 km s^{-1} as compared to a velocity increase from 6.6 to 7.1 km s^{-1} in our model. The lower velocities in the middle and lower crust of the Holbrook (1990) model result in a 2 km shallower crust–mantle transition zone, although the shape of this layer is similar to ours with a northward-deepening trend. Also, the crust–mantle transition layer thickens toward the north as in our model, but the increase is from 1.5 to 3 km as compared to 2 to 4 km in our model. The thinner transition layer may explain the slightly lower velocities of 7.7 to 7.8 km s^{-1} in the upper mantle as compared to 7.9 km s^{-1} in our model.

These comparisons have confirmed that the same general features of the *P*-wave crustal structure are present in the various models, within the limitations discussed at the beginning of this section. The main advantages of our inversion algorithm as compared to some or all of the other forward and inverse methods used in the comparison studies are (1) 2-D velocity structure is obtained, (2) a flexible model parametrization and an efficient method of ray tracing is used, (3) the inversion for velocity and interface position can be performed simultaneously, (4) estimates of model parameter uncertainty, resolution and non-uniqueness are provided, and (5) the additional constraint offered by amplitude data can be incorporated into the model.

The differences in the velocities, depths and thicknesses of comparable features in the five final models suggests the following absolute parameter uncertainties for the north–south line of the Nevada PASSCAL data: ±0.2 km s^{-1} for velocities and ±2 km for boundary depths. The variability of the lower crustal velocity and average Moho depth between the models, as well as parameter trade-offs, were tested using the absolute parameter uncertainty estimation technique discussed earlier. An uncertainty of ±0.25 km s^{-1} was obtained for the lower crustal *P*-wave velocity and results in a ±2 km variation in average Moho depth.

7 DISCUSSION

An inverse technique for obtaining 2-D velocity structure from traveltime data has been presented that allows for simultaneous determination of velocities and layer boundaries. One advantage of simultaneous inversion is that it allows the trade-off between all model parameters to be quantified. The method is applicable to any *P*- and/or *S*-wave data since the initial step of the inversion is equivalent to trial-and-error forward modelling. In that sense, the method may be viewed as an automated forward modelling approach. However, it can also be used to efficiently interpret large, multishot data sets, such as the 1986 Nevada PASSCAL data, that are not amenable to a conventional trial-and-error forward modelling approach.

The effectiveness of this inverse technique is due to a model parametrization that is suited to the requirements of an inverse approach where the number and position of velocity and boundary nodes can be suited to the data's subsurface ray coverage. The forward step uses a robust method of ray tracing and as such the inversion algorithm benefits from the advantages of ray methods. A simulation of smooth layer boundaries increases the stability of the inversion by permitting more of the observed data to be used in the inversion by extending traveltime branches and reducing geometrical shadow zones. Boundary smoothing is accomplished with a three-point averaging filter, but could also be achieved using a low-pass frequency filter with a cut-off based on the dominant wavelength of the observed data.

The inversion algorithm is primarily intended for multishot crustal refraction/wide-angle reflection data typical of modern seismic experiments. These data normally have a limited shot and/or receiver spacing that does not allow a model parametrization consisting of a uniform grid of velocity points with a spacing fine enough to adequately represent the true velocity field, as in conventional tomography, since these data can well resolve relatively fewer model parameters. There are a number of reasons why the inversion algorithm as presented is best suited to typical crustal data. First, although our model parametrization can accommodate a finely spaced uniform rectangular velocity grid, it allows for features that are necessary when modelling typical wide-angle crustal data: (1) velocity discontinuities, (2) an irregular spacing and number of velocity and boundary nodes within each layer, and (3) the incorporation of constraints provided by amplitude modelling. Second, we have chosen to avoid the use of model smoothing or a set of empirical rules restricting parameter adjustment at each iteration that is necessary as the number of model parameters becomes large since the amount of constraint on each parameter decreases and the degree of lateral heterogeneity potentially increases, making it less likely that rays can be traced to all observation points. Finally, we seek a model with a minimum number of independent parameters because ray tracing in general becomes increasingly unstable as the model heterogeneity increases. In addition, increased heterogeneity results in increasingly non-uniform ray coverage within the model so that the dependence of the final model on the starting model and, therefore, the potential non-uniqueness of the final model, increases. This is because traveltime inversion is a non-linear problem requiring a starting model that is 'close' to the true model and this becomes less likely as the heterogeneity of the final model increases.

When the algorithm is applied to typical crustal seismic data, we found it necessary to run a series of inversions to determine the optimum number and location of velocity and boundary nodes that provide the best trade-off between RMS traveltime residual and parameter resolution, and also allows rays to be traced to all observations. For high-quality data with relatively small picking uncertainties, it will generally not be possible to achieve χ^2 values near one. This is because data with low spatial density may be unable to resolve the small-scale features that the data have sampled. For the five-shot north–south line of the Nevada PASSCAL experiment, the P_g phase has an average pick uncertainty of ±0.04 s and a corresponding final χ^2 value of 12.9, whereas the P_cP phase has a higher average pick uncertainty of ±0.17 s but a lower χ^2 value of 1.2.

Due to the inherent non-linearity of the traveltime

inversion problem, model parameter values and surface ray coverage must be examined after each iteration. It may be necessary to hold poorly constrained parameters fixed if their values become unrealistic or prevent rays to be traced to all observation points. In particular, velocity reversals with depth are often removed manually since they can cause large shadow zones at the surface within which the observed data have been picked. Note that if velocity reversals exist within the true model, the inversion algorithm can determine these as well as any other model feature assuming their signature is present within the inverted traveltimes. It may be necessary to adjust the damping for certain iterations to obtain the lowest possible RMS traveltime residual. It is sometimes necessary to hold fixed the vertical velocity gradient or layer thickness, perhaps based on the results of amplitude modelling, of layers with an inadequate coverage or angular distribution of ray paths to improve the stability of the inversion.

A seismic arrival of any type that can be forward modelled can be included in the inversion scheme. This includes refracted, reflected and head wave arrivals as well as multiple and surface reflections. Using the same approach, it would be straightforward to calculate the necessary partial derivatives to invert *S*-wave and *P–S* converted arrivals for Poisson's ratio. Pseudo-diffracted ray paths could be used to invert non-geometrical arrivals, i.e. the weak arrivals within a shadow zone, or arrivals that lie within a geometrical shadow zone that is an artifact of the ray method, i.e. caused by model blockiness. It would be straightforward to extend the algorithm to perform a simultaneous inversion for 3-D structure using data consisting of intersecting linear profiles and common model parameters at intersection points. Thus, 3-D structure could be inferred from in-line shot data inverted using 2-D models and 2-D ray tracing. Finally, the inversion algorithm can be used during experiment planning to determine optimal shot–receiver geometries.

The benefits of using amplitude data to provide more detailed velocity structure than is possible with traveltime data alone has been demonstrated in many studies using conventional trial-and-error forward modelling. Amplitude information was used indirectly in the inversion of the PASSCAL data presented here, since it provided estimates of velocity gradients in some model layers and the evidence for and velocity within the crust–mantle transition layer. This additional constraint probably resulted in a final model closer to the 'true' model than would have been possible otherwise.

To directly incorporate amplitude data into the present inversion framework would potentially be very useful. It may be possible to calculate the partial derivatives of amplitude with respect to vertical velocity gradients and velocity discontinuities at boundaries, either analytically or numerically, and thereby include amplitude data in the inversion. However, given the difficulty of recording reliable amplitude information in crustal experiments, particularly on land, the potential advantage of including amplitude information may be limited. As with conventional forward modelling, only the general trends of amplitude variations or the relative average amplitudes of different phases may be considered. A greater problem may be the inherent inaccuracy of ray amplitudes. Theoretical amplitudes could be calculated with the reflectivity or finite difference method and combined with the partial derivatives calculated by ray tracing. If amplitudes are considered, it may be necessary to incorporate or invert for Q^{-1} (attenuation) structure.

ACKNOWLEDGMENTS

CAZ was supported by a Natural Sciences and Engineering Research Council of Canada Postdoctoral Scholarship with supplementary support provided by an IRIS (Incorporated Research Institutions for Seismology) grant to the University of Utah. The 1986 Nevada PASSCAL experiment was funded by the National Science Foundation through IRIS, the US Geological Survey, and the Air Force Geophysical Laboratory. Computing was performed on a SUN Sparc server, funded in part by the AMOCO Foundation, and on workstations of the Crustal Seismology group, Department of Geology and Geophysics, University of Utah. J. A. Braun kindly provided the traveltime picks and associated uncertainties used in the 1986 Nevada PASSCAL data example and W. S. Holbrook provided a preprint of his paper. CAZ thanks W. C. Nagy, D. J. Trentman and A. Z. Ahmed for teaching him about SUN computers. H. M. Benz and B. C. Zelt provided critical reviews of an earlier version of the paper. The thorough reviews of the submitted manuscript by R. B. Hawman and an anonymous reviewer also improved the paper. B. C. Zelt and C. M. Jarchow suggested improvements to the computer code.

REFERENCES

Aki, K. & Richards, P. G., 1980. *Quantitative Seismology*, vol. 2, Freeman, San Francisco.

Benz, H. M., Smith, R. B. & Mooney, W. D., 1990. Crustal structure of the northwestern Basin and Range province from the 1986 Program for Array Seismic Studies of the Continental Lithosphere seismic experiment, *J. geophys. Res.*, **95**, 21 823–21 842.

Boland, A. V. & Ellis, R. M., 1989. Velocity structure of the Kapuskasing uplift, northern Ontario, from seismic refraction studies, *J. geophys. Res.*, **94**, 7189–7200.

Braun, J. A. & Smith, R. B., 1989. Two-dimensional inversion for crustal structure using refraction/wide-angle reflection data from the 1986 PASSCAL Basin-Range experiment, *EOS, Trans. Am. geophys. Un.*, **70**, 1206.

Catchings, R. D. & Mooney, W. D., 1988. Crustal structure of the Columbia Plateau: evidence for continental rifting, *J. geophys. Res.*, **93**, 459–474.

Červený, V., Molotkov, I. & Pšenčík, I., 1977. *Ray Method in Seismology*, University of Karlova, Prague, Czechoslovakia.

Firbas, P., 1987. Tomography from seismic profiles, in *Seismic Tomography*, pp. 189–202, ed. Nolet, G., Reidel, Dordrecht.

Hawman, R. B., Colburn, R. H., Walker, D. A. & Smithson, S. B., 1990. Processing and inversion of refraction and wide-angle reflection data from the 1986 Nevada PASSCAL experiment, *J. geophys. Res.*, **95**, 4657–4691.

Henry, W. J., Mechie, J., Maguire, P. K. H., Khan, M. A., Prodehl, C., Keller, G. R. & Patel, J., 1990. A seismic investigation of the Kenya Rift Valley, *Geophys. J. Int.*, **100**, 107–130.

Holbrook, W. S., 1990. The crustal structure of the northwestern Basin and Range province, Nevada, from wide-angle seismic data, *J. geophys. Res.*, **95**, 21 843–21 869.

Huang, H., Spencer, C. & Green, A., 1986. A method for the inversion of refraction and reflection travel times for laterally varying velocity structures, *Bull. seism. Soc. Am.*, **76**, 837–846.

Lutter, W. J. & Nowack, R. L., 1990. Inversion for crustal structure using reflections from the PASSCAL Ouachita experiment, *J. geophys. Res.*, **95**, 4633–4646.

Lutter, W. J., Nowack, R. L. & Braile, L. W., 1990. Seismic imaging of upper crustal structure using travel times from the PASSCAL Ouachita experiment, *J. geophys. Res.*, **95**, 4621–4631.

McMechan, G. A. & Mooney, W. D., 1980. Asymptotic ray theory and synthetic seismograms for laterally varying structures: theory and application to the Imperial Valley, California, *Bull. seism. Soc. Am.*, **70**, 2021–2035.

Menke, W., 1984. *Geophysical Data Analysis: Discrete Inverse Theory*, Academic Press, Orlando.

PASSCAL Working Group, 1988. The 1986 PASSCAL Basin and Range lithospheric seismic experiment, *EOS, Trans. Am. geophys. Un.*, **69**, 596–598.

Press, W. H., Flannery, B. P., Teukolsky, S. A. & Vetterling, W. T., 1986. *Numerical Recipes: The Art of Scientific Computing*, Cambridge University Press, Cambridge, UK.

Sheriff, R. E. & Geldart, L. P., 1983. *Exploration Seismology, vol. 2: Data Processing and Interpretation*, Cambridge University Press, Cambridge, UK.

Spence, G. D., 1984. Seismic structure across the active subduction zone of western Canada, *PhD thesis*, University of British Columbia.

Spence, G. D., Whittall, K. P. & Clowes, R. M., 1984. Practical synthetic seismograms for laterally varying media calculated by asymptotic ray theory, *Bull. seism. Soc. Am.*, **74**, 1209–1223.

Spence, G. D., Clowes, R. M. & Ellis, R. M., 1985. Seismic structure across the active subduction zone of western Canada, *J. geophys. Res.*, **90**, 6754–6772.

Tarantola, A., 1987. *Inverse Problem Theory*, Elsevier, Amsterdam.

Zelt, C. A. & Ellis, R. M., 1988. Practical and efficient ray tracing in two-dimensional media for rapid traveltime and amplitude forward modelling, *Can. J. expl. Geophys.*, **24**, 16–31.

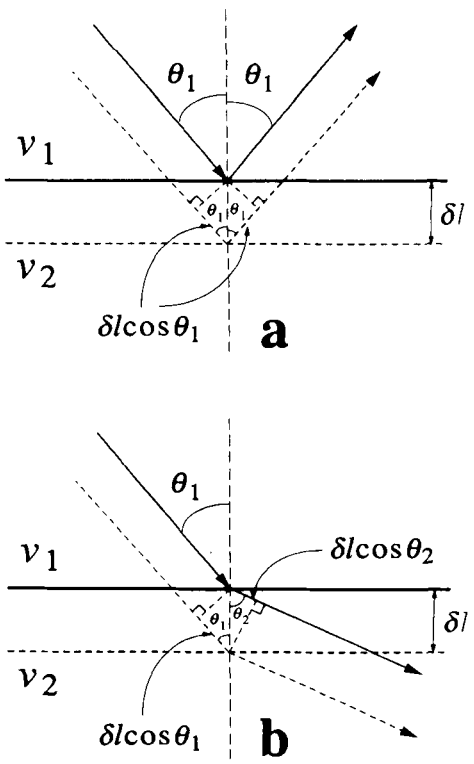

Figure A1. Reflected (a) and refracted (b) ray at a boundary that has been moved downward in a perpendicular direction to the boundary by a small amount, δl. The angle of incidence is θ_1 and the angles of reflection and refraction are θ_1 and θ_2, respectively. The velocities above and below the boundary are v_1 and v_2. The increased path length is $2\delta l \cos\theta_1$ and $\delta l(\cos\theta_1 - \cos\theta_2)$ for the reflected and refracted ray, respectively.

APPENDIX

Consider a reflected and refracted ray at a boundary before and after the boundary has been moved downward a small distance, δl (Fig. A1). For the reflected ray, the increased path length is $2\delta l \cos\theta_1$, so that the extra traveltime is

$$\delta t = \frac{2\delta l \cos\theta_1}{v_1}$$

and the partial derivative becomes

$$\frac{\partial t}{\partial l} = \frac{2\cos\theta_1}{v_1}. \tag{A1}$$

Similarly for the refracted ray, the partial derivative is

$$\frac{\partial t}{\partial l} = \frac{\cos\theta_1}{v_1} - \frac{\cos\theta_2}{v_2}. \tag{A2}$$

Note that (A2) is more general since it reduces to (A1) if θ_2 is measured from the normal below the boundary. We require the derivatives in (A1) and (A2) to be calculated with respect to a small vertical adjustment, δz, at the endpoints of the boundary. Consider Fig. A2 in which the left endpoint is shifted downward while the right endpoint remains fixed. The vertical change in the position of the boundary at the point x, δh, is related to change normal to the boundary, δl, by the angle α given by the equation

$$\frac{\delta l}{\delta h} = \cos\alpha. \tag{A3}$$

The vertical change at x, δh, is related to the change at the

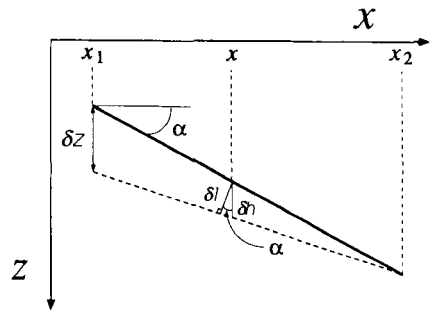

Figure A2. A boundary with endpoints at x_1 and x_2 and angle α with respect to the horizontal, is moved downward a small distance δz at the left endpoint. The relationship between the vertical change in the position of the boundary at x, δh, and the change normal to the boundary, δl, is given by (A3).

boundary endpoint, δz, according to the equation

$$\frac{\delta h}{\delta z} = \frac{x_2 - x}{x_2 - x_1}. \tag{A4}$$

Similarly, if the right endpoint is shifted upward while the left endpoint remains fixed,

$$\frac{\delta h}{\delta z} = \frac{x - x_1}{x_2 - x_1}. \tag{A5}$$

If we define $\Delta x = x_2 - x$ for a left endpoint shift, $\Delta x = x - x_1$ for a right endpoint shift, and $\Delta x_b = x_2 - x_1$, then (A4) and (A5) can be written as

$$\frac{\delta h}{\delta z} = \frac{\Delta x}{\Delta x_b}. \tag{A6}$$

Using the chain rule and (A2), (A3) and (A6), the general expression for the boundary node partial derivative is

$$\frac{\partial t}{\partial z} = \left(\frac{\cos\theta_1}{v_1} - \frac{\cos\theta_2}{v_2}\right) \cos\alpha \left(\frac{\Delta x}{\Delta x_b}\right).$$